Heat and Mass Transfer (2023) 59:2181–2195
https://doi.org/10.1007/s00231-023-03403-6

ORIGINAL ARTICLE

Thermal analysis of suspended single droplet evaporation measurements with a coupled lumped parameter model

Dávid Csemány[1]

Received: 14 March 2023 / Accepted: 13 July 2023 / Published online: 19 July 2023

Abstract

The measurement data of single droplet evaporation experiments are often biased due to the extra heat input through the fiber suspension and the presence of thermal radiation in hot environments. This encumbers model validation for heat and mass transfer simulations of liquid droplets. In this paper, a thermal analysis of this measurement layout is presented with a coupled lumped parameter model, considering heat conduction through the suspension. The model was validated by experimental data from the literature and good agreements were found. The thermal analysis focused on fiber material and geometry, and thermal radiation properties. Calculations were performed on a broad range of ambient conditions for liquids with different volatility characteristics. Temporal squared droplet diameter- and temperature-profiles, furthermore, droplet stationary evaporation rate were used to characterize vaporization phenomena. The thermal balance of the droplet is dominated by the convective heat rate from the environment in the early stage of evaporation. The effect of heat conduction through the fiber becomes important at the end of the droplet lifetime when the droplet size is decreased. Temperature sensor suspension may seriously bias droplet temperature due to the larger thermal conductivity compared to quartz fiber. Large droplets in high-temperature environments show significant sensitivity to thermal radiation properties, which should be considered in measurements and model validation.

Nomenclature

Latin letters

B	Spalding number, 1
c_p	Specific heat capacity at constant pressure, J/(kg·K)
D	Mutual diffusion coefficient, m^2/s
d	Diameter, m
g	Gravitational acceleration, m/s^2
Gr	Grashof number, 1
h	Heat transfer coefficient, $W/(m^2 \cdot K)$
k	Thermal conductivity, W/(m·K)
L	Latent heat of evaporation, J/kg
l	Length, m
Le	Lewis number, 1
M	Molecular mass, kg/kmol
m	Mass, kg
Nu	Nusselt number, 1
p	Pressure, Pa
Pr	Prandtl number, 1
Pt	Platinum, -
$\dot{Q}$	Heat rate, W
Ra	Rayleigh number, 1
Re	Reynolds number, 1
Sc	Schmidt number, 1
SiO_2	Quartz, -
T	Temperature, K
u	Relative velocity, m/s
Y	Mass fraction, 1

Greek symbols

β	Thermal expansion coefficient, 1/K
ε	Emissivity, 1
λ	Evaporation rate, m^2/s
μ	Dynamic viscosity, Pa·s
ρ	Density, kg/m^3
Σ	Sum of atomic and structural diffusion volume Increment, 1
φ	View factor, 1

Indices

0	Initial value
∞	Ambient value

✉ Dávid Csemány
csemany@energia.bme.hu

[1] Department of Energy Engineering, Faculty of Mechanical Engineering, Budapest University of Technology and Economics, Műegyetem Rkp. 3., Budapest 1111, Hungary

a	Air
conv	Convective
d	Droplet
evap	Evaporation
f	Fiber
g	Vapor-ambient gas mixture
L	Liquid
M	Mass transfer
n-e	Non-evaporating
rad	Radiation
ref	Reference
s	Surface
st	Stationary
T	Heat transfer
total	Total
v	Vapor

1 Introduction

Transportation is the largest source of greenhouse gas (GHG) emissions in the European Union. Concerning passenger or light-duty transportation, electric vehicles represent a maturing technology. The question here is the source of electricity production and the long-term environmental impact of battery technology. Heavy-duty transportation, including shipping, aviation, and road freight, has a 46% share in the GHG emissions of transportation [1]. Consequently, alternative powertrains are necessary to achieve deep decarbonization. However, heavy-duty transportation has strict constraints on cargo space and payload, therefore, energy sources with high energy density are required to provide economic operation. Consequently, conventional and renewable liquid fuels will remain in the portfolio in the foreseeable future [2], which necessitates heat and mass transfer simulations in engine design. However, calculations must be validated by experimental results.

Comprehensive measurement data on single droplet evaporation is available in the literature. There are measurement layouts, where the droplet is deposited on a hot surface [3, 4]. However, most experimental setups can be categorized into two groups: stagnant suspended droplet and falling droplet, both aim to obtain the temporal evolution of droplet diameter. Several experimental datasets are published corresponding to the stagnant suspended droplet method for liquids with significantly different fuel properties. Among others, these include n-alkanes, like n-heptane [5–7], n-decane [8, 9], n-hexadecane [10], vegetable oils [11], jet fuel [12], water and emulsions [13, 14], and binary mixtures containing polar and non-polar components [15]. The reason for the prevalence of this layout is that the effect of forced convection on droplet evaporation can be eliminated since the droplet is stagnant. Therefore, the influence of thermophysical and transport properties of the fuel can be evaluated independently of operating conditions. Moreover, the optical apparatus detecting the temporal evolution of droplet size can be arranged conveniently and spherical symmetry of the droplet can be provided at a reasonable level. Despite its advantages, the setup has several drawbacks. Thermal radiation may affect the rate of droplet evaporation due to the high-temperature wall of the measurement section and the hot ambient gas. Furthermore, the droplet is fixed to a fiber suspension or temperature sensor. In the latter case, the temporal variation of droplet temperature can be detected. However, both cases seriously affect the thermal balance of the droplet since the suspension has a significantly higher thermal conductivity than the vapor–gas mixture around the droplet surface. Therefore, it acts as an additional heat input, intensifying evaporation.

To overcome the bias in the thermal balance of suspended droplet, the evaporation process of falling droplets is also measured. However, systematic experimental data for a wide range of ambient pressure and temperature is rare in the literature due to the more problematic arrangement of optical apparatus [16]. The velocity of the ambient gas is adjusted, resulting in a low relative velocity between the falling droplet and the gas flow. In this manner, the effect of forced convection enhancing evaporation can be decreased. However, thermal radiation can remain important due to the hot surfaces of the measurement chamber.

The present paper focuses on the suspended droplet measurement method since this layout is used more frequently. However, a systematic evaluation of its thermal biases is missing. Figure 1 summarizes the concept of a typical experimental setup based on ref. [11]. A pressure regulator and a temperature controller operating a heating rod are used to adjust the ambient pressure and temperature in the measurement chamber. High temperature may lead to droplet burning, therefore, inert gas, which is usually nitrogen, is used to avoid oxidation and focus on heat and mass transfer phenomena. The droplet is placed to the suspension with a thin needle before insertion into the chamber, then it is moved inside with a droplet elevator operated by a stepper motor. In order to avoid preliminary droplet heat-up, the inlet of the chamber is cooled with water in a closed cycle. The optical access to the measurement position is provided by glass windows on the sidewalls. Backlight is applied from one side and the temporal variation of droplet size is recorded from the other side with a high-speed camera, thus binary images are obtained from the droplet by adjusting the threshold. Data is collected with a proper data acquisition (DAQ) device and transferred to a computer for post-processing. The pixel to distance conversion is done by calibration with a known object. After detecting the droplet boundary in the processed images, a high-order polynomial is fitted to it. Rotational symmetry is assumed and the volume of the droplet is determined. The

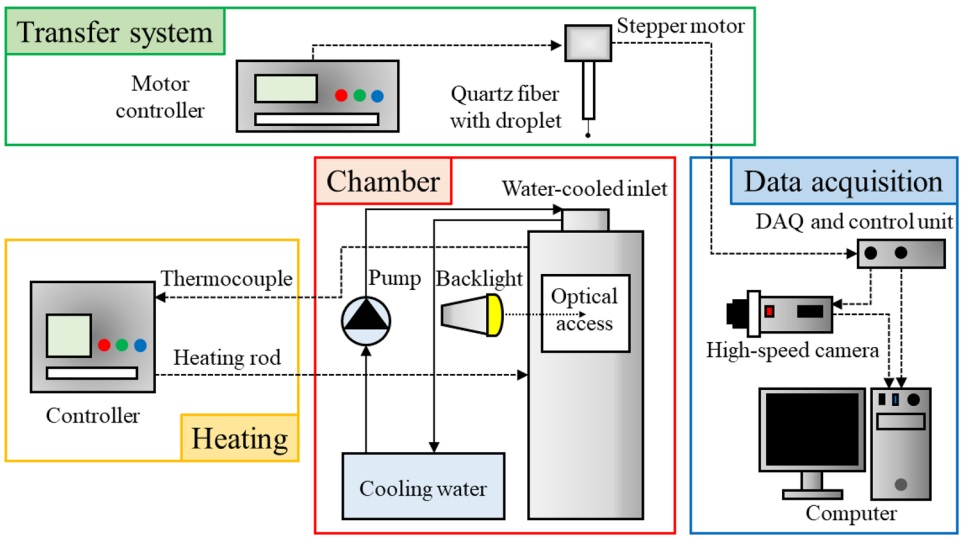

Fig. 1 Concept of a typical experimental setup for stagnant suspended droplet evaporation measurement based on ref. [11]

diameter of the droplet is the diameter of a sphere equivalent in volume. Spherical symmetry is a cornerstone in most droplet evaporation models. To preserve this shape, an aircraft moving on a parabolic flight or a free-falling capsule, containing the suspended droplet can be used to carry out experiments. However, they are very expensive and therefore limited in the literature. Another difficulty is that the stable vapor boundary around the droplet obstacles evaporation in microgravity environment [10].

It is rather challenging to quantify the total uncertainty of the experiments. However, it is important to highlight the most important biasing factors, affecting the measured temporal variation of droplet size. The rotational symmetry may be violated due to the presence of the suspension. Curve fitting to the boundary of the droplet in the processed images is also a source of uncertainty due to the resolution of the images. Yang and Wong [17] reported an average $\pm$ 15 µm uncertainty, which is 1.5% of the initial diameter and 2.7% of the diameter at the end of the measurement. Despite the water-cooled inlet, an uncontrolled heat-up of the suspended droplet may occur at the beginning of the experiments. Moreover, temperature sensors have larger thermal conductivity than quartz fibers, which can result in the further enhancement of the extra heat input.

The additional heat to the droplet through the fiber suspension enhances vaporization, thus, it can seriously affect model validation. Consequently, this effect should be considered. Generally, two concepts are used for this correction. The first one introduces an empirical correction factor to the stationary evaporation rate [7]. The stationary evaporation rate characterizes the temporal surface decrease of the droplet and it is discussed in the next section. Correction factors are determined in terms of fiber suspension diameter for measurements under identical conditions. The reference data corresponds to the smallest fiber diameter and cross-fiber suspension arrangements are usually used for this purpose [7]. This method can provide sufficient corrections, however, the empirical factors are confined to the experimental setup and ambient conditions. In the other method, the additional heat is considered as a source term in the thermal balance of the droplet. Several modeling concepts exist for this purpose, like lumped parameter modeling [18], one-dimensional approaches [13, 17, 19], and multi-dimensional approaches [20–23]. However, systematic analyses on a broad range of ambient conditions, fuel volatility, and suspension material and geometry are scarce in the literature. Therefore, the novelty and the aim of this paper is to fill this gap with a coupled lumped parameter modeling approach to provide a sufficient estimate of the general thermal biasing effects in single droplet evaporation measurements. The focus is on constructing a model with reasonable computational demand applicable for comprehensive parameter analysis. Experimental data is used to evaluate the model and quantify its limitations. Focusing on qualitative, rather than quantitative thermal analysis, general recommendations can be made for further model validation and measurement planning. The applied and tested evaluation methodology of this analysis can be the base for further advanced models. Moreover, droplet evaporation models are also used in non-combustion-related fields corresponding to different ambient condition range [24], further necessitating the thermal evaluation of droplet vaporization measurements used for validation. The coupled model is presented in the next section.

2 Suspended droplet evaporation model

The thermal balance of the suspended droplet with the various heat sources and the main concept of the evaporation model are presented in Fig. 2. The fiber is horizontal and

the immersed part of it is equal to the instantaneous droplet diameter. Both the thermal balance of the droplet and that of the fiber suspension are considered as lumped parameter models, indicated by the red contours in Fig. 2. No temperature distribution is considered inside the droplet and along the fiber. The droplet surface temperature, T_s, is concentrated to the droplet center. The fiber temperature, T_f, corresponds to the dry surface of the suspension and only that part is considered in its thermal balance since the dry part is significantly longer than the immersed part. Coupling between the droplet and the fiber thermal balances is performed via the conduction heat rate, $\dot{Q}_f$. Generally, the temperature of the fiber increases more rapidly due to its lower heat capacity (~10^4 J/K for ~1 cm long SiO_2 fiber [5, 25]). This results in a temperature difference between the fiber and the droplet during the evaporation process.

The key equations of the numerical model are presented next. The model was implemented into Matlab R2022a environment. All the liquid- and vapor-phase thermophysical and transport properties of the evaporating droplet are pressure- and temperature-dependent, acquired from the National Institute of Standards and Technology (NIST) database [25]. The following equations are solved in each time-step. Two components are considered in the gas phase: fuel vapor and ambient gas. Vapor-ambient gas mixture properties, like specific heat capacity at constant pressure, c_{pg}, thermal conductivity, k_g, dynamic viscosity, μ_g, and density, ρ_g, are calculated for T_{ref} reference temperature and $Y_{v,ref}$ reference vapor mass fraction according to the considerations detailed in ref. [26], assuming ideal mixing when Dalton's law and Amagat's law are valid and the conditions are far from critical. Vapor-phase properties are calculated for T_{ref}, while liquid-phase properties correspond to the droplet temperature. Equations (1) and (2), solved with the explicit second-order Adams–Bashforth method, describe the thermal balances of the droplet and fiber suspension, respectively:

$$m_d c_{p,L} \dot{T}_s = \dot{Q}_{conv,d} - \dot{Q}_{evap} + \dot{Q}_f + \dot{Q}_{rad,d} \tag{1}$$

$$m_f c_f \dot{T}_f = \dot{Q}_{conv,f} - \dot{Q}_f + \dot{Q}_{rad,f} \tag{2}$$

where m_d is the droplet mass, $c_{p,L}$ is the liquid-phase specific heat capacity at constant pressure, and T_s is considered uniform inside the droplet. Overdot means time derivative. $\dot{Q}_{conv,d}$, $\dot{Q}_{evap}$, and $\dot{Q}_{rad,d}$ are the convective heat rate from the environment to the droplet, heat rate of vaporization, and radiative heat rate from the environment to the droplet, respectively. m_f is the fiber mass, c_f is the specific heat capacity of fiber material, while $\dot{Q}_{conv,f}$ and $\dot{Q}_{rad,f}$ are the convective heat rate from the environment to the fiber and radiative heat rate from the environment to the fiber. The

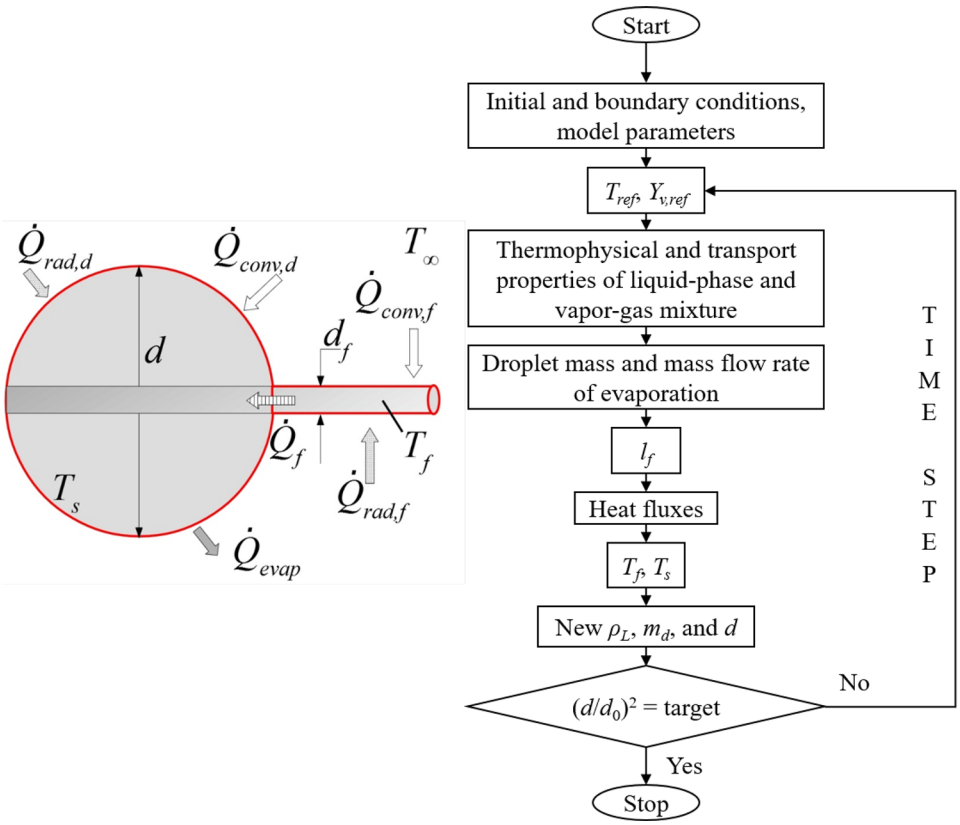

Fig. 2 (Left) Thermal balance of the suspended droplet setup and (right) the main concept of the evaporation model

convective heat rate from the environment to the droplet is calculated as:

$$\dot{Q}_{conv,d} = -h_d d^2 \pi \left(T_s - T_\infty\right) \tag{3}$$

where h_d is the heat transfer coefficient between the droplet and surrounding gas, d is the droplet diameter and T_∞ is the ambient gas temperature. The heat rate of vaporization is calculated as:

$$\dot{Q}_{evap} = \dot{m}_d L \tag{4}$$

where $\dot{m}_d$ is the mass flow rate of evaporation and L is the latent heat of vaporization. The latter is determined with the Watson equation [27]. The conduction heat rate from the fiber, considering circular cross-section can be written as:

$$\dot{Q}_f = -k_f \frac{d_f^2 \pi}{4} \cdot \frac{T_s - T_f}{d/2} \tag{5}$$

where k_f, and d_f are the fiber thermal conductivity and fiber diameter. The instantaneous distance between the center of the droplet and the free surface of the fiber is represented by $d/2$. The radiative heat rate from the environment to the droplet is considered as:

$$\dot{Q}_{rad,d} = d^2 \pi (\varepsilon\varphi)_d \sigma_0 \left(T_{rad}^4 - T_s^4\right) \tag{6}$$

where $(\varepsilon\varphi)_d$ describes the emissivity of the droplet and the view factor for the measurement configuration, σ_0 is the Stefan-Boltzmann constant, and T_{rad} is the temperature of the radiation heat source. The latter can represent high-temperature measurement chamber walls, cold walls of the room, or ambient gas temperature. The convective heat rate from the environment to the fiber is calculated as:

$$\dot{Q}_{conv,f} = -h_f d_f \pi l_f \left(T_f - T_\infty\right) \tag{7}$$

where h_f is the heat transfer coefficient between the fiber and the environment, while l_f is the instantaneous dry length of the fiber exposed to heat transfer from the environment. The radiative heat rate between the environment and fiber can be calculated as:

$$\dot{Q}_{rad,f} = d_f \pi l_f (\varepsilon\varphi)_f \sigma_0 \left(T_{rad}^4 - T_f^4\right) \tag{8}$$

where $(\varepsilon\varphi)_f$ describes the emissivity of fiber and the view factor for the measurement setup. In accordance with the measurements, the initial droplet diameter is considered as an initial condition. Consequently, the occupied volume of suspension is subtracted from the calculated droplet volume, and the droplet mass is determined as follows:

$$m_d = \rho_L \left(\frac{d^3 \pi}{6} - \frac{d_f^2 \pi}{4} d \right) \tag{9}$$

where ρ_L is the droplet density. The instantaneous dry length of the fiber suspension exposed to the heat transfer from the environment is calculated as:

$$l_f = l_0 + d_0 - d \tag{10}$$

where l_0 and d_0 are the initial dry length of the fiber and initial droplet diameter. The fiber is considered as a horizontal cylinder with d_f diameter and l_f length. h_f is determined from Nusselt number correlations for natural and forced convection. The characteristic length is d_f. The Reynolds number, required in case of forced convection is:

$$\mathrm{Re}_f = \frac{\rho_g \cdot u \cdot d_f}{\mu_g} \tag{11}$$

where u is the relative velocity between the stagnant fiber and the gas flow. For forced convection, the Nusselt number for the fiber is calculated as [28]:

$$\mathrm{Nu}_f = 0.3 + 0.62 \cdot \mathrm{Re}_f^{0.5} \cdot \frac{\mathrm{Pr}^{0.33}}{\left(1 + \left(\frac{0.4}{\mathrm{Pr}}\right)^{2/3}\right)^{0.25}} \cdot \left(1 + \left(\frac{\mathrm{Re}_f}{2.82 \cdot 10^5}\right)^{5/8}\right)^{0.8} \tag{12}$$

while for natural convection, it is calculated as [29]:

$$\mathrm{Nu}_f = \left(0.6 + 0.387 \cdot \left(\mathrm{Ra}_{T,f} \cdot \left(1 + \left(\frac{0.559}{\mathrm{Pr}}\right)^{9/16}\right)^{-16/9}\right)^{1/6}\right)^2 \tag{13}$$

where the Prandtl number is:

$$\mathrm{Pr} = \frac{c_{p,g} \mu_g}{k_g} \tag{14}$$

and the fiber Rayleigh number for heat transfer is:

$$\mathrm{Ra}_{T,f} = \mathrm{Gr}_f \cdot \mathrm{Pr} \tag{15}$$

where the Grashof number for the fiber is:

$$\mathrm{Gr}_f = \frac{g \rho_g \beta \left(T_f - T_\infty\right) d_f^3}{\mu_g} \tag{16}$$

where g and β are the gravitational acceleration and the thermal expansion coefficient of ambient gas. The validity range of Eq. (12) is $0.2 \leq \mathrm{Re}_f$; Pr, while that of Eq. (13) is $0 < \mathrm{Pr} < \infty$. No information is available for Ra_f. The total incoming heat rate of the droplet is defined as:

$$\dot{Q}_{total,d} = \dot{Q}_{conv,d} + \dot{Q}_f + \dot{Q}_{rad,d} \tag{17}$$

In order to calculate the convective heat rate from the environment to the droplet by Eq. (3), h_d needs to be determined with Nusselt number correlations [28–30]. The characteristic

length is the instantaneous droplet diameter. For a stagnant non-evaporating sphere, the Nusselt number is:

$$\mathrm{Nu}_{d,n-e} = 2 + \frac{0.589 \cdot \mathrm{Ra}_{T,d}^{1/4}}{\left(1 + \left(\frac{0.43}{\mathrm{Pr}}\right)^{9/16}\right)^{4/9}} \tag{18}$$

where the droplet Rayleigh number for heat transfer is:

$$\mathrm{Ra}_{T,d} = \mathrm{Gr}_d \cdot \mathrm{Pr} \tag{19}$$

where the Grashof number for the droplet is:

$$\mathrm{Gr}_d = \frac{g\rho_g\beta\left(T_s - T_\infty\right)d^3}{\mu_g^i} \tag{20}$$

The Nusselt number for a non-evaporating sphere in case of forced convection is:

$$\mathrm{Nu}_{d,n-e} = 2 + 0.6 \cdot \mathrm{Re}_d^{1/2} \cdot \mathrm{Pr}^{1/3} \tag{21}$$

where the Reynolds number for the droplet is:

$$\mathrm{Re}_d = \frac{\rho_g \cdot u \cdot d}{\mu_g} \tag{22}$$

The validity range of Eq. (18) is $\mathrm{Ra}_{T,d} \leq 10^{11}$ and $0.7 \leq \mathrm{Pr}$ [28], while Eq. (21) is valid for $0.7 \leq \mathrm{Pr} \leq 400$ and $3.5 \leq \mathrm{Re} \leq 7.6 \cdot 10^4$ [31] (available in Hungarian). The Nusselt number for the droplet, accounting for evaporation, is [30]:

$$\mathrm{Nu}_d = \frac{\ln\left(1 + B_T\right)}{B_T} \cdot \mathrm{Nu}_{d,n-e} \tag{23}$$

The Spalding heat transfer number is:

$$B_T = \left(1 + B_M\right)^{\frac{c_{p,v}}{c_{p,g}} \cdot \frac{1}{\mathrm{Le}}} - 1 \tag{24}$$

where $c_{p,v}$ is the vapor-phase specific heat capacity at constant pressure, and the Lewis number is:

$$\mathrm{Le} = \frac{k_g}{\rho_g D_{v,a} c_{p,g}} \tag{25}$$

characterizing the relation of thermal boundary layer thickness to the concentration boundary layer thickness, where $D_{v,a}$ is the mutual diffusion coefficient of fuel vapor and ambient gas. The Spalding mass transfer number is:

$$B_M = \frac{Y_{v,s} - Y_{v,\infty}}{1 - Y_{v,s}} \tag{26}$$

where $Y_{v,\infty}$ is the mass fraction of vapor in the far field, which is considered zero for the single droplet case. Assuming vapor–liquid equilibrium and ideal gas conditions, the mass fraction of fuel vapor on the droplet surface is:

$$Y_{v,s} = \left(1 + \left(\frac{p_\infty}{p_{v,s}} - 1\right)\frac{M_a}{M_v}\right)^{-1} \tag{27}$$

where p_∞ is the ambient pressure, $p_{v,s}$ is the vapor pressure, acquired from the NIST database, corresponding to T_s, M_a is the ambient gas molecular mass, and M_v is the fuel molecular mass. Accounting for the Stefan flow, the mass flow rate of evaporation is:

$$\dot{m}_d = \mathrm{Sh} \cdot \pi d D_{v,a} \rho_g \ln\left(1 + B_M\right) \tag{28}$$

where overdot means time derivative. In order to calculate the ratio of convective mass transfer rate to diffusion rate, the Sherwood number needs to be determined with the following correlations [28]. The droplet Sherwood number for natural convection is:

$$\mathrm{Sh} = 2 + \frac{0.589 \cdot \mathrm{Ra}_{M,d}^{1/4}}{\left(1 + \left(\frac{0.43}{\mathrm{Sc}}\right)^{9/16}\right)^{4/9}} \tag{29}$$

where the Schmidt number is:

$$\mathrm{Sc} = \frac{\mu_g}{\rho_g D_{v,a}} \tag{30}$$

while the droplet Rayleigh number for mass transfer is:

$$\mathrm{Ra}_{M,d} = \mathrm{Gr}_d \cdot \mathrm{Sc} \tag{31}$$

The droplet Sherwood number for forced convection is:

$$\mathrm{Sh} = 2 + 0.6 \cdot \mathrm{Re}_d^{1/2} \cdot \mathrm{Sc}^{1/3} \tag{32}$$

The mutual diffusion coefficient of fuel vapor and ambient gas is calculated with the method of Fuller et al. [32, 33]:

$$D_{v,a} = \frac{0.00143 \cdot T_{ref}^{7/4}}{p_\infty M_{v,a}^{1/2}\left(\Sigma_v^{1/3} + \Sigma_a^{1/3}\right)^2} \tag{33}$$

where $M_{v,a}$ is the average molar mass of the vapor-ambient gas mixture, while Σ_v and Σ_a are the sums of atomic and structural diffusion volume increments of vapor and ambient gas. Note that Eq. (33) was evaluated with reference data in ref. [34].

The d^2-profile, shown in Fig. 3, characterizing the temporal evolution of droplet size is acquired by solving the equations in each time step. The stationary evaporation rate, λ_{st}, is determined by fitting a line to the range of linear decrease in the d^2-profile. In this manner, λ_{st} characterizes the droplet surface decrease over time. The upper and lower limits of this fitting range are often arbitrary. However, the range of $0.15 \leq (d/d_0)^2 \leq 0.5$ is frequently used [10]. Note

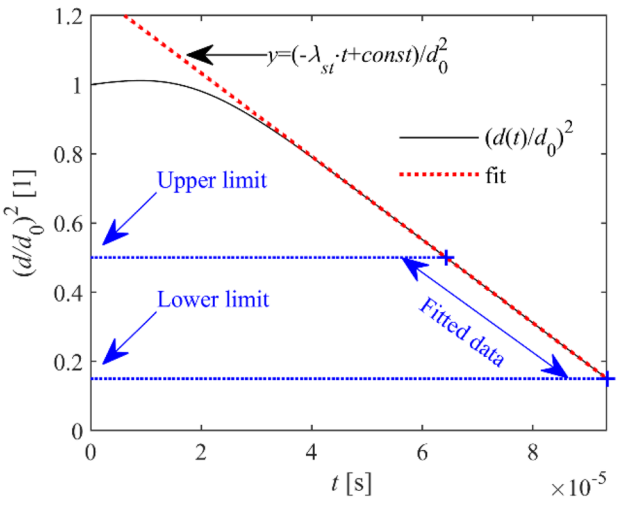

Fig. 3 Obtaining the stationary evaporation rate from the temporal d^2-profile of the droplet

that the lower boundary is usually limited by the experimental setup and droplet deformation, therefore, higher values may be applied. The corresponding range of fitting is $0.3 \leq (d/d_0)^2 \leq 0.5$ for the results presented in this paper. If d^2 data are free from bias, the decrease corresponding to the stationary evaporation phase is linear. Therefore, the upper limit can be higher, as well (e.g., $(d/d_0)^2 = 0.7$). However, if fiber suspension is present, the limits of the fitting should be always provided in details since they can affect the numerical value of λ_{st} due to the possible non-linear trend of the d^2-profile resulting from the extra heat input. Furthermore, when the Knudsen number, relating the mean characteristic free path of the molecules to the droplet radius, is larger than 0.01, the gas phase cannot be regarded as a continuum and kinetic effects should be taken into account. This can be important at the final stage of evaporation or in the case of µm scale droplets generated by modern atomizers. In the case of the currently analyzed droplet size and ambient condition regime, the gas phase can be approximated as a continuum. For further details on kinetic modeling of droplet heating and evaporation, please see ref. [30].

3 Results and discussion

Section 3.1 presents the validation of the numerical model against experimental data obtained from the literature. Next, the results of the thermal analysis, focusing on various features of the experimental setup are discussed in Section 3.2.

3.1 Model validation

The presented model was validated against experimental data of Nomura et al. [5], Yang and Wong [17], and Harada et al. [20] since the initial and boundary conditions and several details of their measurements are accurately discussed. These are summarized in Table 1. However, initial fiber temperature values were not detailed directly. Therefore, it was assumed identical to the initial droplet temperature, $T_{s,0}$. Next, the features of each experimental setup are summarized and the comparison of measurement data and the results of the model are presented.

The published experimental results of Nomura et al. [5] are confined to a measurement chamber with an 80 mm inner diameter and 260 mm height. The ambient gas was nitrogen to prevent droplet burning. Four windows with a 20 mm diameter each provided visual access to the droplet. The ambient gas was heated by an electric furnace inside the chamber. N-heptane droplet was placed on the tip of a silica fiber (SiO_2, $k_f = 1.4$ W/(m·K) [35]), which was moved to the desired position by a droplet elevator. The insertion process required 0.16 s, which may led to an uncontrolled slight preheating of the droplet. T_∞ was measured with a thermocouple 4 mm above the test position. A microgravity

Table 1 Initial and boundary conditions of the reference measurements for model validation

	Nomura et al. [5]	Yang and Wong [17]	Harada et al. [20]
Fuel	n-heptane	n-heptane	n-dodecane
d_0 **[µm]**	700	1000	900
$T_{s,0}$ **[K]**	300	300	314
T_∞ **[K]**	471, 555, 648, 741	490	773
p_∞ **[bar]**	1	1	1
u **[m/s]**	0	0.7	0
d_f **[µm]**	150	50, 150, 300	50
l_0 **[cm]**	1	1	0.05
k_f **[W/(m·K)]**	1.4	1.4	71
g **[m/s^2]**	0	9.81	9.81
Ambient gas	nitrogen	air	air
T_R **[K]**	471, 555, 648, 741	300	773

environment was used to perform the measurements. The tests were carried out in towers with a height of 5 m and 110 m and parabolic flights were used, as well, to acquire the desired conditions. The whole apparatus with the suspended droplet was covered to eliminate drag force and was placed in the tower, which was evacuated to low pressure. After the setup started to fall, the droplet was introduced. The experimental setup was fixed to the floor of an aircraft in the case of parabolic flights. After microgravity conditions were achieved, the droplet was introduced. The evaporation process was recorded with a CCD camera. Droplet diameter was determined according to the concept discussed earlier in Fig. 1, assuming spherical symmetry.

The comparison of the experimental data of Nomura and the results of the model is presented in Fig. 4. Note that the time scale is divided by d_0^2 in accordance with the original published data. Solid lines indicate $(\varepsilon\varphi)_d = 1$, while dashed lines indicate $(\varepsilon\varphi)_d = 0$ to account for the uncertainty of $(\varepsilon\varphi)_d$. The former assumes the black body behavior of the droplet and considers the unity view factor, meaning that all the heat radiation from the environment reaches the droplet. The second extreme situation neglects thermal radiation. Obviously, $0 \le (\varepsilon\varphi)_d \le 1$ condition is valid. Consequently, these boundaries should contain the experimental data. Note that the results showed no significant sensitivity to $(\varepsilon\varphi)_f$ from the thermal balance of the fiber. Therefore, the effect of possible droplet transparency on the absorbed thermal radiation of fiber suspension was neglected in further calculations. The uncertainty of droplet insertion is indicated by the horizontal error bars. Model results show good agreement with reference data. In the case of $(\varepsilon\varphi)_d = 1$, the average

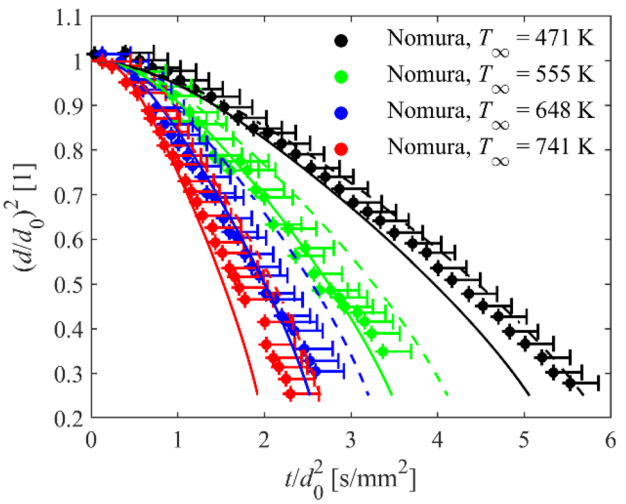

Fig. 4 Comparison of experimental data of Nomura et al. [5] and results of the model. Boundary and initial conditions are presented in Table 1. Solid lines correspond to $(\varepsilon\varphi)_d = 1$, while dashed lines correspond to $(\varepsilon\varphi)_d = 0$. Uncertainty due to droplet insertion is indicated by the horizontal error bars

relative deviation values are 8%, 7%, 7%, and 9% for 471 K, 555 K, 648 K, and 741 K, respectively. The possible influence of thermal radiation is indicated by higher deviation values at higher temperatures, when this phenomenon is neglected since thermal radiation is proportional to T^4. The values are 7%, 22%, 31%, and 25% for 471 K, 555 K, 648 K, and 741 K, respectively.

A hot laminar gas flow generated by an electric heater was used in the experiments of Yang and Wong [17]. The experimental analysis aimed to investigate the influence of suspension diameter on vaporization. Quartz (silica) fibers with 50 µm, 150 µm, and 300 µm were used and placed in the uniform laminar flow provided by a convergent nozzle. The published uncertainty of temperature measurement was 2 K due to thermal radiation and it was neglected in further calculations. Before the measurements, the droplet was protected from the hot gas flow by a water-cooled shield. At the beginning of the experiment, the shield was withdrawn and the droplet was exposed to the flow. The transient temperature history of the hot flow was also measured and the data was published, making it available for model validation. Flow velocity was measured, as well, with Laser Doppler Anemometry. However, no data was available for model validation. A high-speed camera at a framing rate of 500 fps was used to record the vaporization process. The droplets were considered ellipsoids and the reported uncertainty of diameter values was within ± 15 µm.

Figure 5 presents the comparison of the experimental data of Yang and the results of model calculations. Due to the absence of hot surfaces around the droplet, thermal radiation was neglected, thus, only dashed lines are present. The model provides reasonable accuracy since the calculations slightly underpredict droplet lifetime. However, the transient velocity history of gas flow was not considered in the model, which led to higher h_d and enhanced evaporation. For 50 µm, 150 µm, and 300 µm, the average relative deviation between measurement data and calculations are 13%, 21%, and 15%, respectively.

Harada et al. [20] used a Pt-13%Rh/Pt thermocouple (Pt, $k_f = 71$ W/(m·K)) [36] for the suspension of n-dodecane droplets. The fiber diameter was 50 µm. An alumina protection tube covered a significant part of the sensor. The ambient temperature was adjusted with an electric furnace. The droplet was suspended and placed in a water-cooled probe. Then the whole setup was inserted into the test position and the probe was moved away before the measurement. 1000 fps frame rate was used for the high-speed camera to record the images. The droplet diameter was calculated from the area of an equivalent circle.

Figure 6 presents the comparison of experimental data of Harada and model calculations. Blue color corresponds to the d^2-profile, while the red color indicates droplet temperature. Solid lines represent $(\varepsilon\varphi)_d = 1$, while dashed lines indicate that thermal radiation is neglected. Therefore, radiative heat

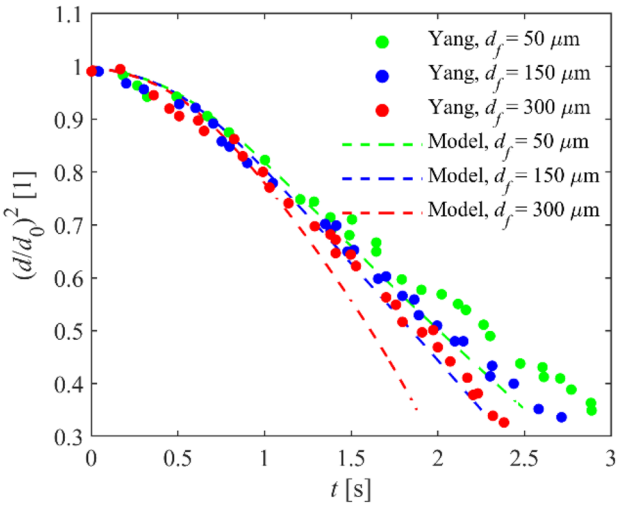

Fig. 5 Comparison of experimental data of Yang and Wong [17] and results of the model. Boundary and initial conditions are presented in Table 1. Dashed lines correspond to $(\varepsilon\varphi)_d = 0$

transfer was considered as a sensitivity parameter again. A reasonable agreement can be observed with measurement data, similar to the multidimensional model of Harada. However, in their model, Harada rightly points out that the heat transfer between the suspension and droplet through the contact surface is a rate-determining factor and the corresponding heat transfer coefficient is a crucial parameter. Unfortunately, the literature has very limited information on accurately determining this coefficient, therefore, it is a potential future work. Note that the stationary evaporation phase is significantly influenced by radiation, indicated by the solid red line. On the other hand, this effect is less

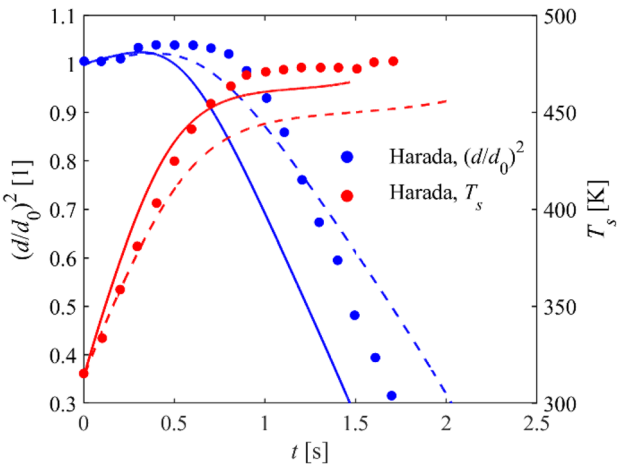

Fig. 6 Comparison of experimental data of Harada et al. [20] and results of the model. Boundary and initial conditions are presented in Table 1. Solid lines correspond to $(\varepsilon\varphi)_d = 1$, while dashed lines correspond to $(\varepsilon\varphi)_d = 0$

obvious from the d^2-profile. It is also important to highlight that the higher k_f of the thermocouple leads to increasing droplet temperature in the stationary evaporation phase. l_f was considered in accordance with the protection tube. The average relative deviation values of the d^2-profile are 22% and 31% for neglecting thermal radiation and $(\varepsilon\varphi)_d = 1$, respectively, and 18 K and 10 K, for the temperature-profiles, respectively. Overall, sufficient accuracy is provided by the coupled lumped parameter model.

3.2 Thermal analysis

Various features of the experimental setup, affecting the droplet thermal balance, are evaluated next with the presented numerical model. N-alkanes from n-hexane to n-dodecane, except for n-nonane and n-undecane, were analyzed to cover a broad range of fuel volatility. Furthermore, these compounds are often considered in experiments. High-fidelity data for their pressure- and temperature-dependent thermophysical and transport properties are available in the NIST database [25], therefore, the uncertainty resulting from these properties can be minimized. Nitrogen was considered as ambient gas in accordance with the experiments focusing on mass transfer phenomena. No gas flow was considered, therefore, Eqs. (13), (18) and (29) were used for the corresponding calculations, accounting for natural convection. It was assumed that the droplet was inserted into the measurement chamber while it was already suspended, therefore, the initial droplet and fiber temperatures were uniformly 300 K. The fiber material was quartz (SiO_2).

The share of different heat sources in the total heat rate, defined by Eq. (17), is presented in Fig. 7a. Characteristics of n-hexane and n-dodecane are compared to present the effect of fuel volatility. Blue color corresponds to n-hexane, while red color refers to n-dodecane. Figure 7b indicates the boundary conditions. Thermal radiation is considered with $(\varepsilon\varphi)_d = 0.5$. The droplet lifetimes are significantly different, thus, the time scale is non-dimensional. ${t_d}^2{}_{30\%}$ is the time elapsed until d^2 reduces to 30% of ${d_0}^2$. Due to the larger droplet size at the beginning of the evaporation process, $\dot{Q}_{conv,d}$ dominates. As vaporization progresses, the surface area of the droplet reduces due to mass transfer, thus, the share of convective heat rate decreases. However, depending on the experimental layout, droplet size, and ambient temperature, the share of thermal radiation increases, then decreases due to the reduction of droplet size. This is in agreement with the findings of Harada et al. [20]. N-hexane is more volatile than n-dodecane, therefore, its droplet size decrease is faster than that of n-dodecane under identical conditions, resulting in a steeper decrease of $\dot{Q}_{conv,d}$ at the beginning of the process and an earlier maximum of $\dot{Q}_{rad,d}$. In the early stage of evaporation, the share of $\dot{Q}_f$ is marginal.

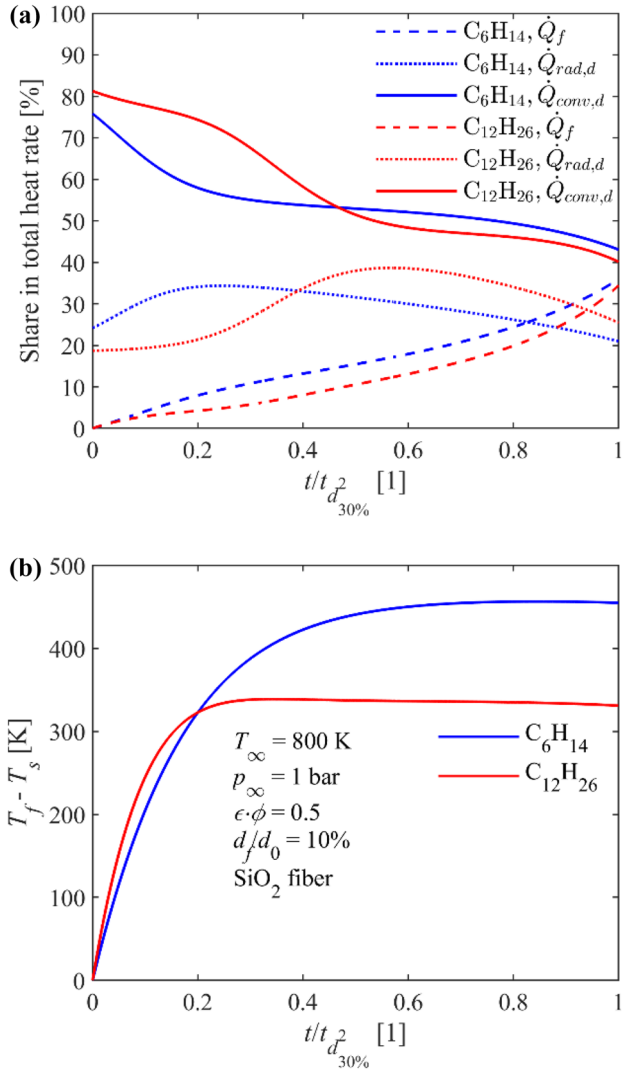

Fig. 7 **a** Share of the different sources in the total incoming heat rate and **b** temperature difference between fiber suspension and droplet for n-dodecane (red) and n-hexane (blue)

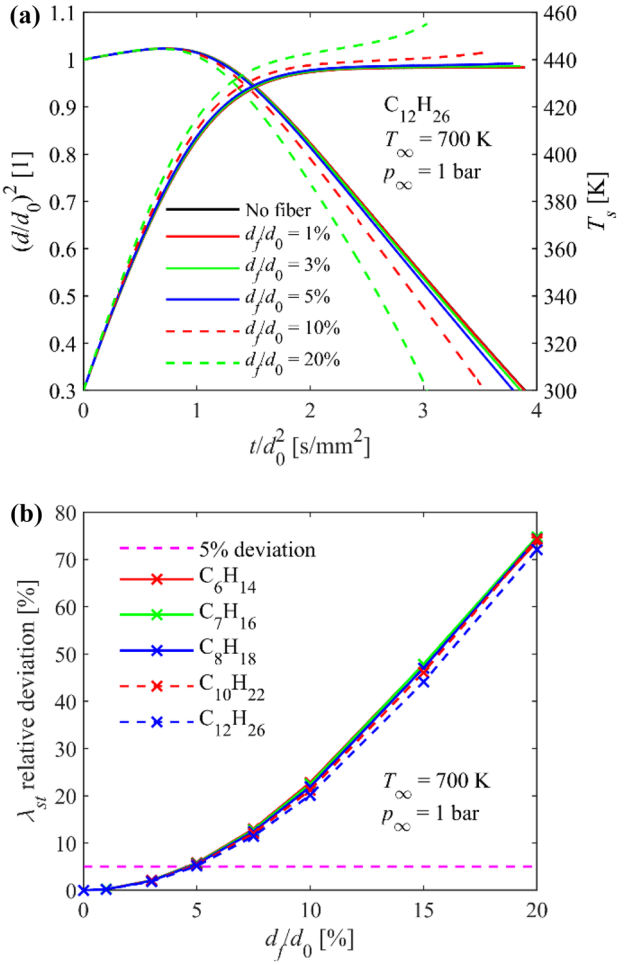

Fig. 8 Effect of fiber diameter-to-initial droplet diameter ratio on the **a** d^2-profile and droplet temperature for n-dodecane and **b** relative deviation of stationary evaporation rate for various n-alkanes. Thermal radiation is neglected

However, as d decreases due to mass transfer, its share increases significantly by the end of the process. Therefore, the stationary evaporation rate is seriously affected. Consequently, d_f/d_0 is a crucial parameter in measurements. $\dot{Q}_f$ for n-hexane possesses a slightly higher share than that of n-dodecane. The reason is the following. N-hexane is more volatile and the temperature difference between the fiber and the droplet in the stationary evaporation regime is higher, shown in Fig. 7b. However, this effect is not significant. Due to the notable temperature difference between the fiber and the droplet, a significant temperature gradient occurs along the fiber, which is the most important limitation of the applied modeling approach for the fiber and the main reason for the qualitative rather than quantitative analysis.

As it was highlighted, d_f/d_0 is an important parameter of experimental layouts. Therefore, its effect on evaporation characteristics is discussed next. To focus on the effect of heat conduction through the suspension, thermal radiation is neglected this time. $l_0 = 1$ cm was considered in the analysis and no notable effect of l_0 was recognized since the effect of d_f is more dominant. Temporal d^2- and droplet temperature-profiles are presented in Fig. 8a with no suspension and for different d_f/d_0 ratios for an n-dodecane droplet at typical experimental conditions. The time scale is divided by d_0^2 in accordance with several published experimental data, like in Fig. 4. As d_f/d_0 is increased, droplet temperature increases too, and droplet lifetime decreases. The relative deviation of λ_{st} with respect to the case without fiber is presented in Fig. 8b in the function of d_f/d_0 for the investigated n-alkanes at the same ambient conditions, which are presented in the figures. The 5% deviation value is highlighted with the dashed line. Fuels with different volatility show practically

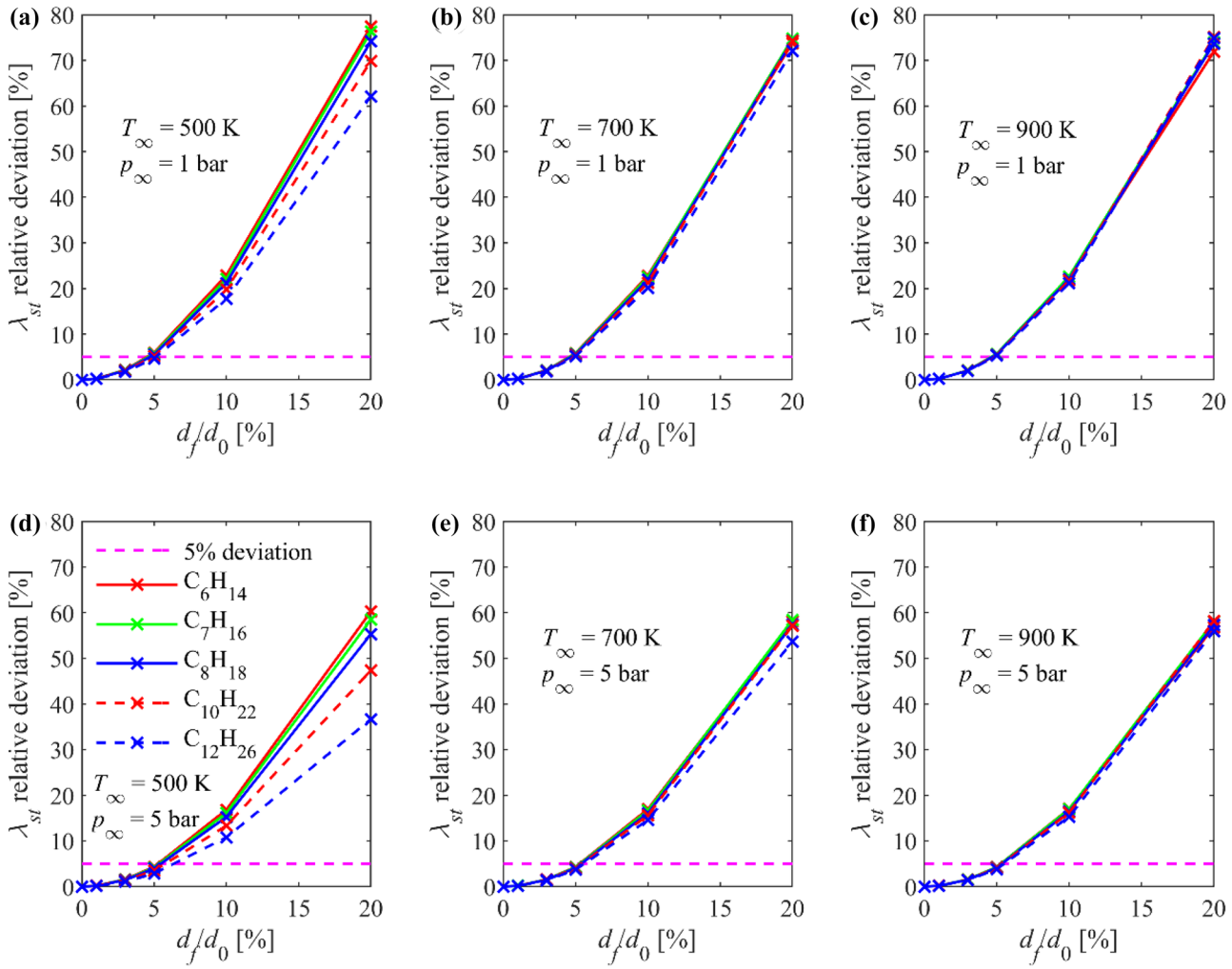

Fig. 9 Effect of fiber diameter-to-initial droplet diameter ratio on the relative deviation of stationary evaporation rate at different ambient conditions (**a**, **b**, and **c** correspond to 1 bar and 500 K, 700 K, and 900 K, respectively, while **d**, **e**, and **f** correspond to 5 bar and 500 K, 700 K, and 900 K, respectively) for various n-alkanes. Thermal radiation is neglected

the same trends. The relative deviation of λ_{st} increases moderately up to $d_f/d_0 = 5\%$. Above that limit, a steeper increase can be observed, thus droplet vaporization has higher sensitivity to d_f in that range. Harada et al. [20] also reports that the temperature deviation increases linearly with increasing d_f.

The effect of d_f/d_0 on the relative deviation of λ_{st}, extended to a wider ambient condition range for the investigated n-alkanes, is presented in Fig. 9 for 500 K, 700 K, and 900 K gas temperature and for 1 bar and 5 bar ambient pressure. The 5% deviation is indicated with a dashed line again. The relative deviation notably increases with fuel volatility at $T_\infty = 500$ K since the difference between T_f and T_s is higher, as detailed in Fig. 7. 500 K is a frequent lower limit for the gas temperature in experiments. Increasing T_∞ diminishes the effect of fuel volatility and the different n-alkanes show practically matching trends. For $d_f/d_0 < 5\%$, the relative deviation stays below 5%. 900 K is a typical upper limit for the gas temperature in experiments. The effect of p_∞ is the following. The boiling point of the droplet increases with pressure, therefore, the stationary evaporation phase can be characterized by a higher T_s. However, T_f is not influenced by p_∞ and their difference decreases. This leads to a decrease in $\dot{Q}_f$, resulting in a decrease in the relative deviation, shown in Fig. 9d–f, compared to Fig. 9a–c. Consequently, increasing pressure decreases the effect of thermal bias through the fiber. If thermal radiation is considered in the thermal balance of the droplet, λ_{st} without fiber increases due to enhanced vaporization. Therefore, the sensitivity of λ_{st} on d_f/d_0 decreases.

Quartz (SiO_2) is the typical suspension material in experiments. However, if droplet temperature is of interest, thermocouples or resistance temperature detectors (RTDs) with extremely small diameters are used the acquire temperature data and act as droplet suspension, as well. Platinum (Pt) is a typical material to solder type R thermocouples and

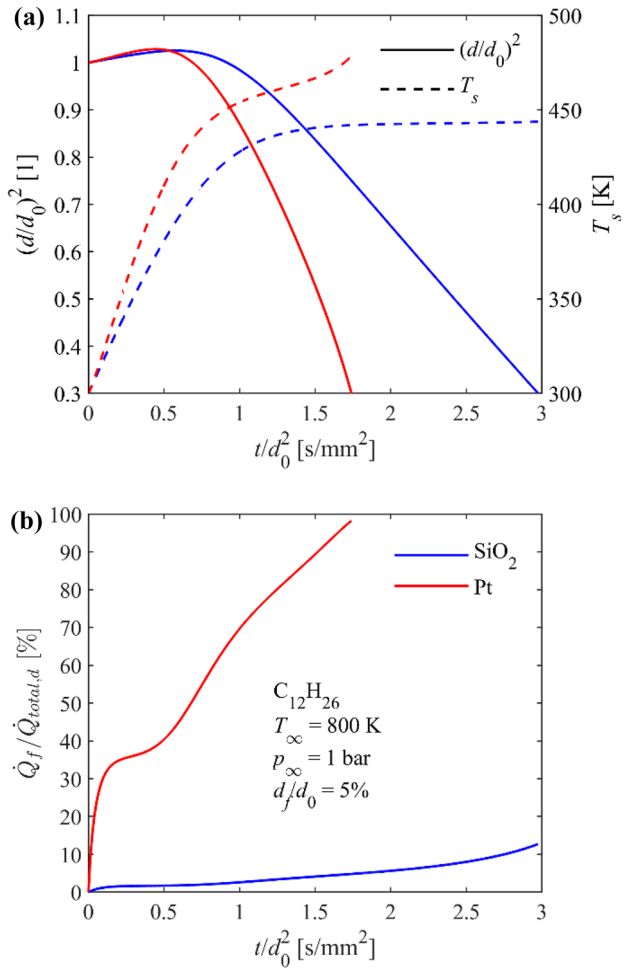

Fig. 10 Effect of fiber suspension material on the **a** d^2-profile and droplet temperature and **b** share of conduction heat rate through the suspension in the total incoming heat rate for an n-dodecane droplet. Thermal radiation is neglected

manufacture RTDs. Note that Harada et al. [20] also used a type R thermocouple to acquire droplet temperature, as discussed in Fig. 6. However, k_f of Pt is a magnitude higher than that of SiO_2, seriously affecting $\dot{Q}_f$. Figure 10a shows the effect of material selection (blue and red colors) on the temporal d^2- and T_s-profiles (solid and dashed lines, respectively) of an n-dodecane droplet, while the share of $\dot{Q}_f$ in the total heat rate is presented in Fig. 10b. The boundary conditions are indicated in Fig. 10b. Thermal radiation is neglected this time. d_f/d_0=5% was considered in order to minimize the effect of $\dot{Q}_f$ as much as possible. Even though the thermal conductivity of Pt is significantly higher than that of SiO_2, their volumetric heat capacities are similar [35, 36]. Droplet lifetime is significantly shorter for Pt and in the stationary regime, T_s is higher by more than 20 K than in the case of quartz fiber. This can seriously affect temperature measurements. Furthermore, no actual stationary state can be observed for the temperature-profile of the Pt case, shown by the increasing red dashed line in Fig. 10a. The thermal balance is dominated by $\dot{Q}_f$ for Pt, shown in Fig. 10b. However, its share remains much lower for SiO_2 during the vaporization process. Consequently, quartz fiber suspension is more favorable and the measured temperature value by the thermocouple suspension can be highly biased.

It is often troublesome to determine $(\varepsilon\varphi)_d$ accurately for the actual experimental layout. However, the effect of thermal radiation significantly depends on the features of the measurement setup, such as T_∞ and d_0. Two typical but extreme conditions are discussed next for an n-dodecane droplet at p_∞=1 bar. Heat conduction through the fiber is neglected this time to focus on the effect of radiative heat transfer. A larger droplet in higher T_∞ and a smaller droplet in lower T_∞ are considered, indicated with red and blue colors in Fig. 11. The curve parameter is $(\varepsilon\varphi)_d$. Figure 11a shows the temporal d^2- and T_s-profiles, while Fig. 11b presents the share of $\dot{Q}_{rad,d}$ in the total heat

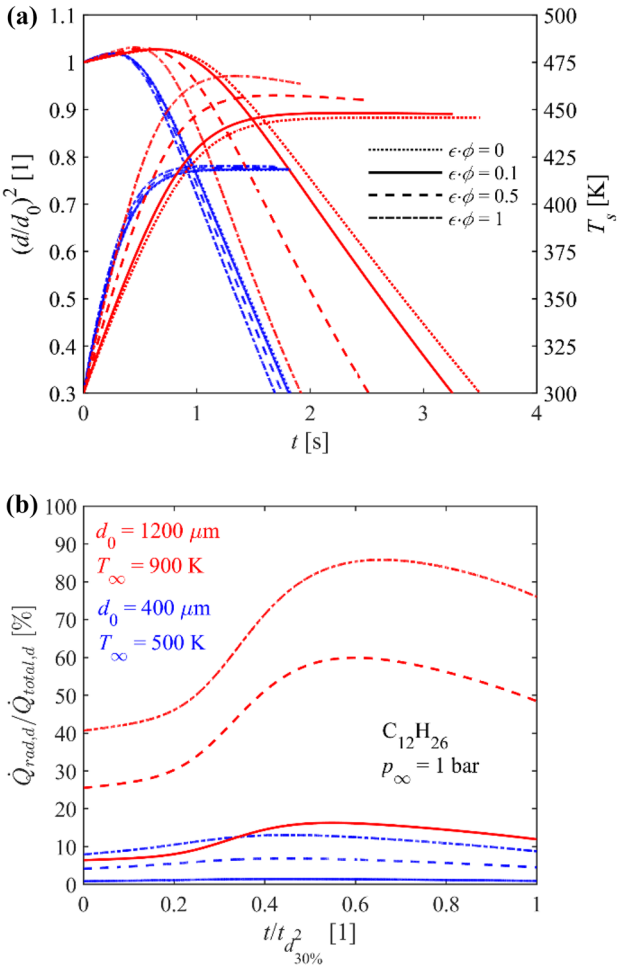

Fig. 11 Effect of emissivity and view factor on the **a** d^2-profile and droplet temperature and **b** share of radiation heat for n-dodecane droplets. Heat conduction through the fiber suspension is neglected. Lines styles distinguish the various emissivity and view factor cases, while red and blue colors represent the different initial droplet sizes and ambient temperature conditions

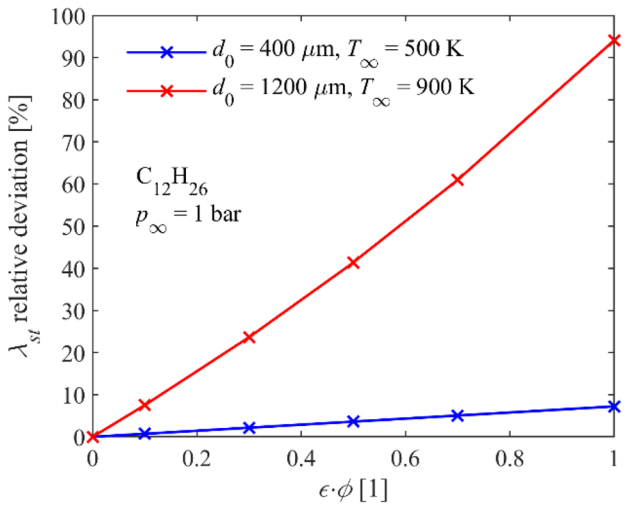

Fig. 12 Effect of emissivity and view factor on the relative deviation of stationary evaporation rate for n-dodecane droplets. Heat conduction through the fiber suspension is neglected

rate, where the time scale is non-dimensional again. The share barely exceeds 10% even for the black body assumption for the lower temperature case. However, the sensitivity is significant to $(\varepsilon\varphi)_d$ for higher temperature and larger droplet size. When black body behavior is assumed, an overshooting tendency can be observed for the larger droplet and higher temperature case, when T_s reaches a maximum and then starts to decrease, as shown in Fig. 11a. This behavior was also reported by Sazhin et al. [37] and by Harada et al. [20], where they attributed this maximum to the contribution of thermal radiation. Figure 12 shows the relative deviation of λ_{st} in the function of $(\varepsilon\varphi)_d$ for the same conditions. The relative deviation remains below 10% for the lower temperature case, however, it exceeds 90% for the high temperature and large droplet case in the extreme $(\varepsilon\varphi)_d$=1 value. Consequently, the uncertainty of $(\varepsilon\varphi)_d$ in typical experimental layouts can notably affect model validation.

4 Conclusions

A detailed thermal analysis of single droplet evaporation measurements was performed with a coupled lumped parameter model by revising the thermal balance of the droplet, accounting for the heat conduction through the fiber suspension. The model was validated against experimental data from the literature, showing reasonable agreement. Besides the temporal squared droplet diameter-, and droplet temperature-profiles, the stationary evaporation rate, λ_{st}, was used as an indicator of vaporization characteristics for evaluation. Characteristics of C_6-C_{12} n-alkanes were analyzed in order to cover a broad range of fuel volatility. Pressure- and temperature-dependent thermophysical and transport properties were obtained from the database of the National Institute of Standards and Technology. Based on the results, the following qualitative conclusions can be derived:

- The thermal balance of the droplet is dominated by the convective heat rate from the hot gas in the early stage of vaporization. As droplet size decreases, the share of conductive heat rate through the quartz suspension increases, notably enhancing vaporization in the stationary evaporation regime.
- The relationship between the quartz fiber diameter-to-initial droplet diameter ratio and the relative deviation of λ_{st} with respect to the case without fiber is non-linear. After a slight increase, a significant rise occurs as the ratio increases. This deviation decreases with increasing ambient pressure due to the increment of droplet boiling temperature.
- Using temperature sensors for suspension can lead to serious bias in droplet temperature due to the typically higher thermal conductivity of the sensor, compared to quartz fiber.
- Concerning thermal radiation, large (mm-scale) droplets in high-temperature environments show high sensitivity to droplet emissivity and view factor of the experimental setup. Consequently, radiative heat transfer should be carefully considered during measurements and model validation.
- The presented coupled lumped parameter model provides reasonable accuracy validated by experimental data from the literature. Consequently, the applied parameter analysis and evaluation method can be the basis of further detailed investigations with more advanced models, where the key factor is the proper definition of the heat transfer coefficient on the contact surface between the suspension and the droplet.

Funding Open access funding provided by Budapest University of Technology and Economics. The research reported in this paper is part of project no. TKP-6–6/PALY-2021, implemented with the support provided by the Ministry of Culture and Innovation of Hungary from the National Research, Development and Innovation Fund, financed under the TKP2021-NVA funding scheme. The research carried out at BME has been also supported by the grant National Research, Development and Innovation Office-NKFIH FK 134277 and by the Sustainable Development and Technologies National Programme of the Hungarian Academy of Sciences (FFT NP FTA).

Declarations

Competing interests The author has no relevant financial or non-financial interests to disclose.

References

1. Gray N, McDonagh S, O'Shea R et al (2021) Decarbonising ships, planes and trucks: An analysis of suitable low-carbon fuels for the maritime, aviation and haulage sectors. Adv Appl Energy 1:100008. https://doi.org/10.1016/j.adapen.2021.100008
2. Balli O, Caliskan N, Caliskan H (2023) Aviation, energy, exergy, sustainability, exergoenvironmental and thermoeconomic analyses of a turbojet engine fueled with jet fuel and biofuel used on a pilot trainer aircraft. Energy 263:126022. https://doi.org/10.1016/j.energy.2022.126022
3. Orzechowski T (2021) Peculiarities in Leidenfrost water droplet evaporation. Heat Mass Transf 57:529–541. https://doi.org/10.1007/s00231-020-02967-x
4. Foudhil W, Chen P, Fahem K et al (2021) Study of the evaporation kinetics of pure and binary droplets: volatility effect. Heat Mass Transf 57:1773–1790. https://doi.org/10.1007/s00231-021-03043-8
5. Nomura H, Ujiie Y, Rath HJ et al (1996) Experimental study on high-pressure droplet evaporation using microgravity conditions. Symp Combust 26:1267–1273. https://doi.org/10.1016/S0082-0784(96)80344-4
6. Verwey C, Birouk M (2018) Experimental investigation of the effect of natural convection on the evaporation characteristics of small fuel droplets at moderately elevated temperature and pressure. Int J Heat Mass Transf 118:1046–1055. https://doi.org/10.1016/j.ijheatmasstransfer.2017.11.038
7. Chauveau C, Birouk M, Halter F, Gökalp I (2019) An analysis of the droplet support fiber effect on the evaporation process. Int J Heat Mass Transf 128:885–891. https://doi.org/10.1016/j.ijheatmasstransfer.2018.09.029
8. Chauveau C, Birouk M, Gökalp I (2011) An analysis of the d2-law departure during droplet evaporation in microgravity. Int J Multiph Flow 37:252–259. https://doi.org/10.1016/j.ijmultiphaseflow.2010.10.009
9. Chauveau C, Halter F, Lalonde A, Gökalp I (2008) An experimental study on the droplet vaporization: effects of heat conduction through the support fiber. In: Proceedings of the 22nd European Conference on Liquid Atomization and Spray Systems
10. Nomura H, Murakoshi T, Suganuma Y et al (2017) Microgravity experiments of fuel droplet evaporation in sub- and supercritical environments. Proc Combust Inst 36:2425–2432. https://doi.org/10.1016/j.proci.2016.08.046
11. Wang J, Wang X, Chen H et al (2018) Experimental study on puffing and evaporation characteristics of jatropha straight vegetable oil (SVO) droplets. Int J Heat Mass Transf 119:392–399. https://doi.org/10.1016/j.ijheatmasstransfer.2017.11.130
12. Yang D, Xia Z, Huang L et al (2018) Exprimental study on the evaporation characteristics of the kerosene gel droplet. Exp Therm Fluid Sci 93:171–177. https://doi.org/10.1016/j.expthermflusci.2017.12.031
13. Strizhak PA, Volkov RS, Castanet G et al (2018) Heating and evaporation of suspended water droplets: Experimental studies and modelling. Int J Heat Mass Transf 127:92–106. https://doi.org/10.1016/j.ijheatmasstransfer.2018.06.103
14. Kim H, Won J, Baek SW (2018) Evaporation of a single emulsion fuel droplet in elevated temperature and pressure conditions. Fuel 226:172–180. https://doi.org/10.1016/j.fuel.2018.04.010
15. Nguyen TTB, Mitra S, Sathe MJ et al (2018) Evaporation of a suspended binary mixture droplet in a heated flowing gas stream. Exp Therm Fluid Sci 91:329–344. https://doi.org/10.1016/j.expthermflusci.2017.10.025
16. Chung SS, Kawaguchi O (1995) Evaporation rate of free paraffin hydrocarbon droplets in a high-temperature and high-pressure gas stream. JSME Int J Ser B 38:121–128. https://doi.org/10.1299/jsmeb.38.121
17. Yang J-R, Wong S-C (2002) An experimental and theoretical study of the effects of heat conduction through the support fiber on the evaporation of a droplet in a weakly convective flow. Int J Heat Mass Transf 45:4589–4598. https://doi.org/10.1016/S0017-9310(02)00164-3
18. Rehman HL, Weiss J, Seers P (2016) Effect of heat conduction on droplet life time and evaporation rate under forced convection at low temperatures. Exp Therm Fluid Sci 72:59–66. https://doi.org/10.1016/j.expthermflusci.2015.10.030
19. Han K, Song G, Ma X, Yang B (2016) An experimental and theoretical study of the effect of suspended thermocouple on the single droplet evaporation. Appl Therm Eng 101:568–575. https://doi.org/10.1016/j.applthermaleng.2015.12.022
20. Harada T, Watanabe H, Suzuki Y et al (2011) A numerical investigation of evaporation characteristics of a fuel droplet suspended from a thermocouple. Int J Heat Mass Transf 54:649–655. https://doi.org/10.1016/j.ijheatmasstransfer.2010.08.021
21. Shringi D, Dwyer HA, Shaw BD (2013) Influences of support fibers on vaporizing fuel droplets. Comput Fluids 77:66–75. https://doi.org/10.1016/j.compfluid.2013.02.005
22. Ghata N, Shaw BD (2014) Computational modeling of the effects of support fibers on evaporation of fiber-supported droplets in reduced gravity. Int J Heat Mass Transf 77:22–36. https://doi.org/10.1016/j.ijheatmasstransfer.2014.04.074
23. Saufi AE, Calabria R, Chiariello F et al (2019) An experimental and CFD modeling study of suspended droplets evaporation in buoyancy driven convection. Chem Eng J 375:122006. https://doi.org/10.1016/j.cej.2019.122006
24. Dadpour D, Lakzian E, Gholizadeh M et al (2022) Numerical modeling of droplets injection in the secondary flow of the wet steam ejector in the refrigeration cycle. Int J Refrig 136:103–113. https://doi.org/10.1016/j.ijrefrig.2022.01.026
25. Lemmon EW, McLinden MO, Friend DG (2019) Thermophysical properties of fluid systems. NIST Chemistry WebBook, NIST Standard Reference Database Number 69
26. Csemány D, Józsa V (2021) A Two-Parameter Corresponding States Method for Calculating the Steady-State Evaporation Rate of C2–C9 n-Alkane Droplets in Air for Elevated Pressures and Temperatures. Flow, Turbul Combust 107:283–305. https://doi.org/10.1007/s10494-020-00238-7
27. Poling BE, Prausnitz JM, O'Connell JP (2001) The Properties of Gases and Liquids, 5th edn. McGraw-Hill, New York, NY, USA
28. Bergman TL, Lavine AS, Incropera FP, DeWitt DP (2017) Fundamentals of Heat and Mass Transfer. Wiley
29. Martin M, Holge K (2010) VDI Heat Atlas, 2nd edn. Springer, Berlin, Heidelberg
30. Sazhin S (2014) Droplets and Sprays, 1st edn. Springer, London
31. Környey T (1999) Hőátvitel, 1st edn. Műegyetemi Kiadó, Budapest
32. Fuller EN, Schettler PD, Giddings JC (1966) New method for prediction of binary gas-phase diffusion coefficients. Ind Eng Chem 58:18–27. https://doi.org/10.1021/ie50677a007
33. Fuller EN, Ensley K, Giddings JC (1969) Diffusion of halogenated hydrocarbons in helium. The effect of structure on collision cross sections. J Phys Chem 73:3679–3685. https://doi.org/10.1021/j100845a020
34. Csemány D, Gujás I, Chong CT, Józsa V (2021) Evaluation of material property estimating methods for n-alkanes, 1-alcohols, and methyl esters for droplet evaporation calculations. Heat Mass Transf 57:1965–1979. https://doi.org/10.1007/s00231-021-03059-0
35. (2020) https://www.iue.tuwien.ac.at/phd/filipovic/node26.html, Silicon Dioxide Properties. https://www.iue.tuwien.ac.at/phd/filipovic/node26.html. Accessed 10 Apr 2020

36. (2020) https://periodictable.com/Elements/078/data.html#Platinum.SpecificHeat.note, Technical data for Platinum. https://periodictable.com/Elements/078/data.html#Platinum.SpecificHeat.note. Accessed 10 Apr 2020
37. Sazhin SS, Kristyadi T, Abdelghaffar WA, Heikal MR (2006) Models for fuel droplet heating and evaporation: Comparative analysis. Fuel 85:1613–1630. https://doi.org/10.1016/j.fuel.2006.02.012